Integrative Biology

Dynamic Article Links

Cite this: *Integr. Biol.*, 2012, **4**, 1428–1436

www.rsc.org/ibiology

PAPER

Comparative study of 3D morphology and functions on genetically engineered mouse melanoma cells†

Ying Zhang,[a] Yuanming Feng,[a] Calvin R. Justus,[b] Wenhuan Jiang,[c] Zhigang Li,[b] Jun Q. Lu,[c] R. Scott Brock,[c] Matthew K. McPeek,[b] Douglas A. Weidner,[d] Li V. Yang*[be] and Xin-Hua Hu*[c]

Received 19th June 2012, Accepted 30th September 2012
DOI: 10.1039/c2ib20153d

Quantification of 3D morphology and measurement of cellular functions were performed on the mouse melanoma cell lines of B16F10 to investigate the intriguing problem of structure–function relations in the genetically engineered cells with GPR4 overexpression. Results of 3D analysis of cells in suspension and phase contrast imaging of adherent cells yield consistent evidence that stimulation of the proton-sensing GPR4 receptor in these cells may modify significantly their morphology with diminishing ability to produce membrane protrusions and to migrate. Examination of the 3D parameters of mitochondria provide further insights on the measured variation of the maximal capacity of oxygen consumption rate among the genetically modified cells, indicating that the proton-sensing receptor may regulate cancer cell metabolism with increased mitochondrial surface area. Our study demonstrates clearly the significant benefits of quantitative 3D morphological study in illuminating cellular functions and development of novel morphology based cell assay methods.

Introduction

It has long been known that differentiated organisms perform their functions with specialized morphologies, *i.e.*, forms and structures, as elegantly discussed by D'Arcy Thompson nearly a century ago.[1] Indeed most classification schemes of biological cells are established on the basis of morphology ranging from leukaemia diagnosis to functional grouping of phytoplankton.[2,3] The enormous advances in molecular biology over recent decades have provided details on the mechanisms underlying the structure–function relation at the molecular levels and stimulate further interests for quantitative knowledge of three-dimensional (3D) morphology. However, 3D study of cell morphology remains very limited, and it is not certain that such a study can be particularly illuminating to important cell biology problems like the effect of genetic modification. For example, investigations of migration and metabolism of cells in response to their microenvironment are essential to the study of tumorigenesis, which is a multi-step process that

[a] *Department of Biomedical Engineering, Tianjin University, Tianjin 300072, China*
[b] *Departments of Internal Medicine and Oncology, Brody School of Medicine, East Carolina University, Greenville, NC 27834, USA. E-mail: yangl@ecu.edu*
[c] *Department of Physics, East Carolina University, Greenville, NC 27858, USA. E-mail: hux@ecu.edu*
[d] *Department of Microbiology and Immunology, Brody School of Medicine, East Carolina University, Greenville, NC 27834, USA*
[e] *Department of Anatomy and Cell Biology, Brody School of Medicine, East Carolina University, Greenville, NC 27834, USA*
† Electronic supplementary information (ESI) available. See DOI: 10.1039/c2ib20153d

Insight, innovation, integration

With development of an accurate image analysis software we demonstrate that quantitative analysis of 3D cell morphology provides critical insights on the migration capability and metabolism of B16F10 cancer cells modified genetically with GPR4 overexpression. Consistent evidence in support of the structure–function relation in the genetically engineered cells has been obtained through an innovative and integrated approach of 3D reconstruction and morphological analysis of suspended cells and functional measurement of attachment and migration of adherent cells. The widely available confocal microscopy resources allow the 3D morphology approach presented here to be extended for investigation of other cellular functions and acquisition of morphological features correlating with light scattering patterns of cells for future development of diffraction imaging flow cytometry.

involves the accumulation of genetic and epigenetic alternations and the somatic evolution of transformed cells largely dictated by the Darwinian principles.[4–6] The interaction between cancer cells and the tumor microenvironment is critical for disease progression as illustrated by the "seed and soil" hypothesis.[7] As a result of gene mutations and somatic evolution, cancer exhibits several distinct hallmarks such as limitless replicating potential, evasion of apoptosis, induction of angiogenesis, tissue invasion and metastasis, deregulated energetic metabolism, and genomic instability.[5] Due to functionally defective blood vessels and glycolytic cancer metabolism, known as the Warburg effect, hypoxia and acidosis are characteristic biochemical features of the tumor microenvironment and play essential roles in cancer somatic evolution and therapeutic responses.[4,6] Nevertheless, the molecular mechanisms by which tumors respond to the acidic microenvironment are poorly understood. In a recent study we have demonstrated that acidosis stimulation of the proton-sensing GPR4 receptor inhibits tumor cell migration and metastasis.[8] Therefore, one would be interested to gain a comprehensive knowledge about the morphological changes in cells allowing the regulation of their migration and metabolism by overexpression of GPR4 in the tumor cells.

Beside its fundamental significance, quantification of 3D morphology can yield powerful criteria of classification for morphology based assay of cells without the need for fluorescent labeling. In an ongoing study of flow cytometry, we have demonstrated the possibility for rapid analysis of different cancer cell lines based on their 3D morphological features by utilizing the strong correlation between cell morphology and texture features of diffraction images.[9–11] Since the diffraction images present the angle-resolved distribution of the light scattered from the single cells excited by a coherent laser beam, the image textures or diffraction patterns are consequence of the intracellular distribution of refractive index or 3D morphology.[12–15] The technique of diffraction imaging has been used in many fields to obtain 3D morphology of particles on the spatial scales commensurate with the wavelengths of the excitation fields, as exemplified by the structural determination of particles ranging from DNA to intracellular organelles with X-ray radiations.[16,17] In the optical frequency domain the morphological features of intracellular organelles are the key elements to determine the diffraction image textures and our recent study has shown that the image textures can be used to classify cells of different morphology.[11] To establish the correlation between cell morphology and diffraction image textures, it is necessary to develop an efficient approach for quantitative extraction and analysis of 3D morphological features as well.

Several imaging methods with 3D capacity have been developed over the last two decades that include, among others, the confocal microscopy, X-ray diffraction microscopy, digital holography or interferometry, optical computed tomography and structured illumination.[17–22] Despite these achievements, quantitative study of 3D morphology is still a venue of infrequent uses to most cell researchers for either scarcity of specialized equipment and/or lack of accurate software tools for rapid reconstruction and analysis. It is thus highly desired to develop an approach for exploration of the full potentials of 3D morphological analysis in cell assay with easy accessibility to instrument, rapid data acquisition, robust reconstruction algorithms and, most importantly, accurate separation of intracellular organelles. For this purpose we have selected the confocal microscopy as the method of 3D imaging for its wide availability and our earlier work of reconstruction related to the modeling study of diffraction images of single cells.[9,14] An improved fluorescent staining protocol and a set of software tools have been developed to perform confocal imaging, 3D reconstruction and quantitative analysis of morphology. In this paper we present a quantitative analysis of 3D cell morphology and functional measurements of the B16F10 cell lines and their genetically engineered variations. The results of the study demonstrate clearly that 3D analysis of cell morphology yields new and valuable insights towards the understanding of the mechanisms underlying regulation of tumor cell migration and metabolism by the proton-sensing GPR4 receptor.

Results

Confocal image stacks were acquired of three types of B16F10 cells, the B16/vector, B16/GPR4 and B16 parental cells, in suspension between glass slides which allow acquisition of image stacks across the whole volume of the cells without interference of the slides. Each cell was randomly selected from an imaged sample and a total of 65 to 67 cells were imaged for each cell type. Selected confocal slice images from one B16/vector cell are shown in Fig. 1 to illustrate the image analysis algorithms. Fig. 2 presents multiple views of two cells' 3D morphology after reconstruction. For quantitative analysis we extracted 31 morphological parameters for all cells in the three groups based on the voxels of 0.070 μm sides in the x–y plane and 0.073 μm side along the z-axis. As expected, the parental cells of B16 display a high degree of similarity in their 3D morphological features with the B16/vector cells as shown by their parameter values in Table 1. In the results presented here, we focus our attention on the differences between the B16/GPR4 cells and B16/vector cells as the control of the genetic modification related to the GPR4 overexpression. Statistical analysis of these parameters was performed with a two-sample t-test to evaluate the significance of the differences between the two cell types of B16/GPR4 and B16/vector and between B16/vector and B16 as a control. Table 1 presents the mean values and standard deviations of selected morphological parameters for each of the three cell groups in additional to the p- values obtained by the t-test method on the set of B16/GPR4 and B16/vector cells (p_{12}) and the set of B16/vector and B16 cells (p_{23}). The definitions of these parameters are given in the notes under the table. The morphological parameters with $p_{12} < 0.05$ in Table 1 are considered to exhibit statistically significant differences between the two cell groups of B16/GPR4 and B16/vector. Based on this criterion it is clear that the B16/GPR4 cells differ in their 3D morphology from the control cells of B16/vector mainly in those associated with the spontaneous protrusions and mitochondria, while the B16/vector cells exhibit high degree of similarity to the B16 cells. Since the cells imaged with confocal microscopy method were detached and kept in suspension, it is intriguing to compare the morphological data against functional measurements of these cells under the adherent condition to investigate their relations.

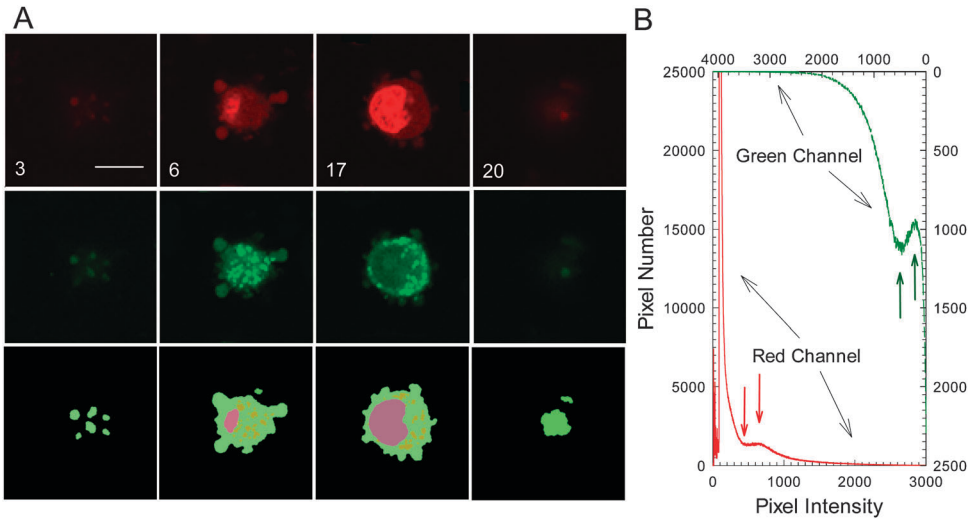

Fig. 1 Raw and segmented confocal slice images acquired from one B16/vector cell (#16): (A) selected raw image slices in the red channel (nucleus and cytoplasm), green channel (mitochondria and cytoplasm) and corresponding segmented images with pixels separated into 4 regions: background (black), cytoplasm (light green), nucleus (dark pink) and mitochondria (dark yellow), the slice sequence number within the stack is marked on each image in the first row; (B) the histograms of pooled pixels of all raw image slices in the red and green channels of the same cell with a pair of arrows indicating the thresholds of I_1 (local minimum) and I_2 (peak) for each channel. Bar = 10 μm.

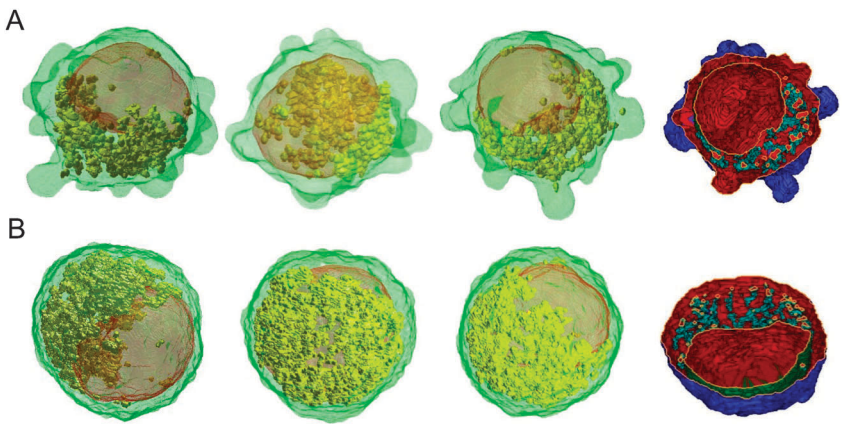

Fig. 2 Different views of the reconstructed 3D cell morphology: (A) three transparent views and one cut-off view of the B16/vector cell (#16); (B) similar views of the B16/GPR4 cell (#22). In transparent (cut-off) views cytoplasm membranes are represented by light green (blue) colors, nuclear membranes by grey-brown (green) colors and mitochondria by dark-green-yellow (light blue) colors.

The comparison study can also prepare the groundwork for future cell assay using the rapid method of diffraction imaging flow cytometry.[9,11,23]

We measured the cell migration and oxygen consumption of the B16/vector and B16/GPR4 cells under the adherent condition. First, the effects of GPR4 on cell attachment and migration were assessed with a time-lapse method using a phase contrast microscope (EVOS, Advanced Microscopy Group). We have previously shown that acidosis stimulation of GPR4 inhibits the migration, invasion and metastasis of B16F10 melanoma cells.[8] Here, the time-lapse microscopy was used to further examine the effects of GPR4 stimulation by acidic pH on cell attachment and migration in real time. In the cell attachment assay at pH 6.4, we noticed that B16/vector cells exhibit a highly dynamic interaction with the substratum (Fig. 3 and Video S1, ESI†). Spontaneously generated protrusions of these cells were observed to make contact with the coverslip surface, and the protrusions extended and retracted dynamically as the components of cell attachment spread and migrate. In contrast, B16/GPR4 cells appeared to generate very few surface protrusions (Fig. 3 and Video S2, ESI†), which is consistent with the 3D results performed on the same type of cells in suspension unveiling much less number of protrusions (Fig. 2 and Table 1). Furthermore, the attachment of B16/GPR4 cells to the coverslip was found to be substantially delayed. By 60 minutes after plating, most B16/vector cells spread out and firmly attached to the coverslip. In comparison the majority of B16/GPR4 cells remained round up with minimal protrusions or spreading as can be seen in Fig. 3 and the Videos S1 and S2 in the (ESI†). We have also used the time-lapse microscopy to assess the effect of GPR4 stimulation by acidic pH on B16F10 cell migration in the wound closure assay which revealed much more detailed information than previously reported using a snapshot method.[8] The time-lapse microscopy results demonstrated that, compared to B16/vector cells, B16/GPR4 cells at pH 6.4 exhibited multiple defects in cell migration (see Fig. 4, Videos S3

Table 1 3D morphological parameters for three types of B16F10 cells[a]

Parameter	Symbol	Unit	Mean ± standard deviation				
			B16/GPR4 (n = 67) [a]	B16/vector (n = 66)	B16 (n = 65)	p_{12}[a]	p_{23}[a]
Cell volume	V_c [b]	μm^3	2987 ± 582	2790 ± 935	2874 ± 886	0.148	0.602
Cell surface area	S_c [c]	μm^2	1422 ± 220	1442 ± 400	1479 ± 370	0.717	0.593
Surface to volume ratio of cell	SVr_c [d]	μm^{-1}	0.4774 ± 0.0509	0.5307 ± 0.06941	0.5279 ± 0.0773	1.4×10^{-6}	0.829
Index of surface irregularity of cell	ISI_c [d]	μm$^{-1/2}$	249.0 ± 22.2	266.8 ± 34.9	273.4 ± 36.9	6.3×10^{-4}	0.295
Average distance of cell membrane voxels to centroid	$\langle R_c \rangle$	μm	8.972 ± 0.598	8.885 ± 1.08	8.953 ± 1.11	0.566	0.725
Standard deviation of R_c	ΔR_c	μm	0.4990 ± 0.213	0.9343 ± 0.643	0.8744 ± 0.595	5.8×10^{-7}	0.581
Number of protrusions	N_p	—	4.820 ± 7.44	13.95 ± 10.5	10.60 ± 11.1	2.3×10^{-6}	0.955
Protrusion volume	V_p	μm^3	99.86 ± 92.8	252.97 ± 157	352.7 ± 333	2.5×10^{-10}	0.037
Nuclear volume	V_n	μm^3	916.8 ± 227	874.1 ± 255	864.6 ± 240	0.310	0.825
Nuclear surface area	S_n	μm^2	692.3 ± 171	655.2 ± 165	647.3 ± 136	0.204	0.764
Index of surface irregularity of nucleus	ISI_n	μm$^{-1/2}$	217.1 ± 20.8	217.2 ± 34.4	218.4 ± 24.1	0.982	0.825
Mitochondrial volume	V_m	μm^3	192.9 ± 64.8	146.6 ± 72.2	149.4 ± 71.0	1.5×10^{-4}	0.823
Mitochondrial surface area	S_m	μm^2	2201 ± 751	1620 ± 1036	1543 ± 778	3.1×10^{-4}	0.632
Surface to volume ratio of mitochondria	SVr_m	μm^{-1}	11.41 ± 0.902	10.75 ± 1.95	10.32 ± 1.95	0.015	0.207
Index of surface irregularity of mitochondria	ISI_m	μm$^{-1/2}$	1495 ± 295	1255 ± 449	1211 ± 341	3.8×10^{-4}	0.528
Distance between the centroids of nucleus and cell	D_{nc}	μm	0.1221 ± 0.0395	0.09668 ± 0.0379	0.1106 ± 0.0379	2.3×10^{-4}	0.037
Volume ratio of nucleus to cell	Vr_{nc}	—	0.3079 ± 0.0564	0.3161 ± 0.0398	0.3048 ± 0.0434	0.331	0.122
Volume ratio of mitochondrion to cell	Vr_{mc}	—	0.06488 ± 0.0186	0.04993 ± 0.0156	0.05141 ± 0.0162	1.8×10^{-6}	0.601

[a] n = number of imaged cells, p_{12} and p_{23} is based on two-sample t-test performed between the B16/GPR4 and B16/vector cells and between B16/vector and B16 cells respectively with highlighted rows are of $p_{12} < 0.05$. [b] $V = N_v V_0$ with N_v as the number of voxels inside the organelle of interest and V_0 as voxel volume. [c] $S = N_s S_0$ with N_s as the number of voxels on the membrane of the organelle and S_0 as the side surface of voxel. [d] ISI $= N_s a_0/(V)^{1/2}$ with a_0 as the side length (= 0.07 μm) of voxel.

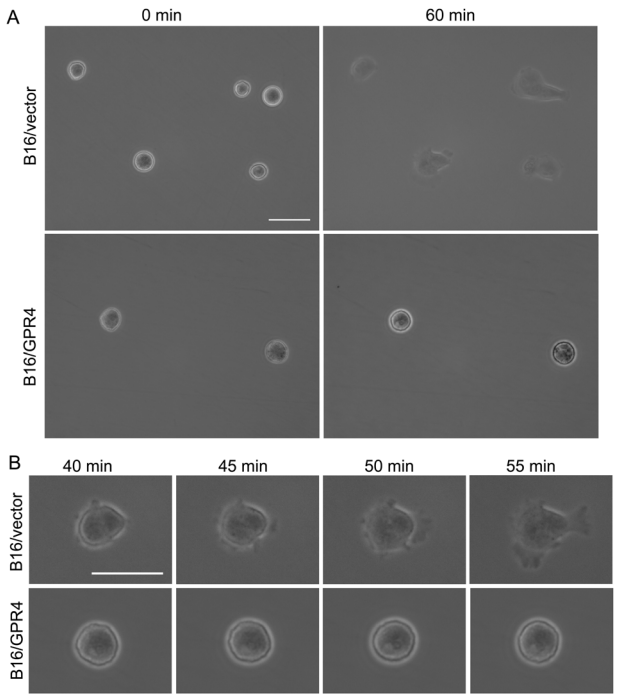

Fig. 3 Time-lapse phase contrast images of cell attachment assay: (A) the attachment analysis of B16/vector cells and B16/GPR4 cells to the coverslip at different time points; (B) the time-lapse view of protrusion formation and spreading of B16/vector and B16/GPR4 cells (with the video file in the ESI†). Bar = 40 μm.

and S4, ESI†). The extension of lamellipodia was impaired, and several divergent leading edges were observed in some B16/GPR4 cells. The detachment and retraction of the tail (trailing edge) of a migrating cell were significantly impaired in B16/GPR4 cells. As a result, B16/GPR4 migrating cells with long un-detached tails were frequently observed. Moreover, fluorescence microscopy of stained actin cytoskeleton showed that, in migrating B16/vector cells treated with pH 6.4, actin is predominantly accumulated in the leading edge. However, in migrating B16/GPR4 cells, actin cytoskeleton existed as bundles of stress fibers as can be observed from the two images presented in Fig. 4(B). Processing and analysis of the time-lapse cell migration images, with selected ones presented in Fig. 4(A), provided the wound width as a functions of recording time as shown in Fig. 4(C) for each cell monolayer. This allowed the calculation of the average migration speeds of cells on the two edges of the wound width before the close of the wound. We found the speed as 59 μm h^{-1} for the B16/vector cells and 5.8 μm h^{-1} for the B16/GPR4 cells migrating at a markedly reduced rate. Taken together, these results suggest that acidosis activation of GPR4 induces a less dynamic actin cytoskeleton, impairs cell protrusion formation, and inhibits cell spreading and migration. Rigorous analysis of the protrusions and other morphological features, however, is impractical with the method of phase contrast microscopy. So we turned to the 3D morphology analysis of suspension cells based on the confocal image stacks.

To fully understand the morphological basis of different migration behaviors, it is useful to extract certain parameters from the 3D imaging study as the metric to quantify the shape of cell membrane which includes the protrusions in both adherent and suspension cells. We chose a distance parameter of R_c defined as the distance between the voxels on the cell surface and centroid of volume for each detached cell measured by the confocal imaging method. A histogram of the cell surface voxel number N_{sc} was generated for each cell with R_c on the horizontal axis, which becomes a delta function for a perfect sphere. In Table 1 the average values of R_c or $\langle R_c \rangle$ among the three cell groups appear very similar to each other

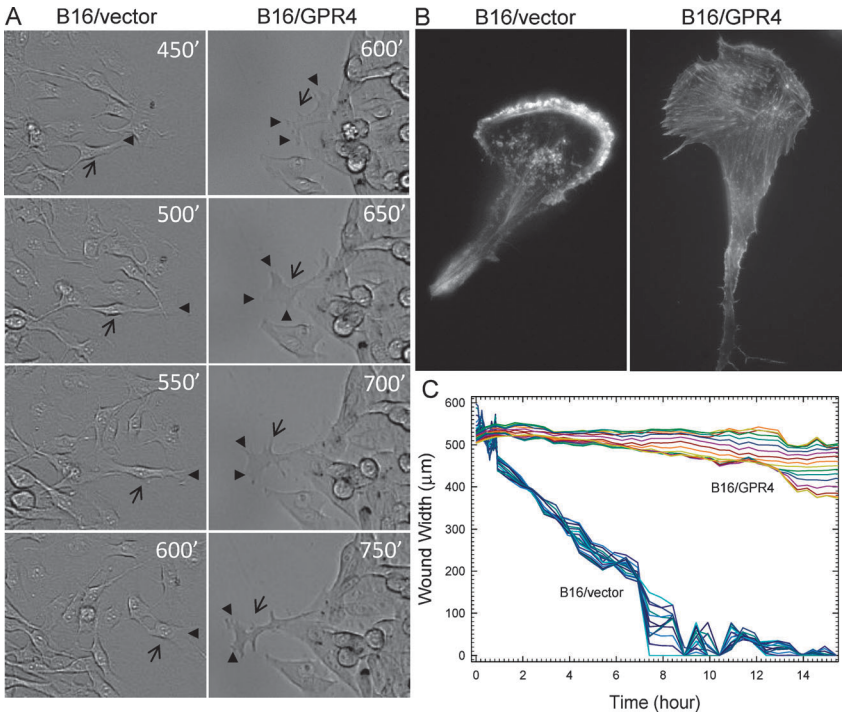

Fig. 4 Time-lapse cell migration assay. (A) The phase contrast images of the migrating B16/vector and B16/GPR4 cells at different times (in minutes) after the wound was generated (with the video file in the ESI†). Arrows indicate representative migrating cells and arrowheads indicate lamellipodia (leading edge) of migrating cells. Please note the divergent lamellipodia of B16/GPR4 cells. (B) The fluorescence images of rhodamine–phalloidin stained actin cytoskeleton of B16/vector and B16/GPR4 cells. (C) The time dependence of wound width sampled from 17 equally spaced bands along the vertical direction of the phase contrast images of migrating B16/vector and B16/GPR4 cells.

in terms of the mean values and standard deviations among all cells in each group. But a close examination of the voxel histograms between the B16/GPR4 and B16/vector cells leads to the fact that these distributions are of distinctive features. As an example, Fig. 5 displays the histograms of 4 cells for each group of the B16/vector and B16/GPR4 cells. The cells in the former group present much longer tails in N_{sc} than those in the latter as R_c increases and thus leads to a larger value of standard deviation calculated from each histogram for each cell as confirmed by the ΔR_c in Table 1. Combined with the protrusion data on each cell type shown in Table 1, these results provide clear evidences to suggest that the B16/vector cells, together with the parental cells of B16, may possess much more dynamic cytoskeletal structures than the B16/GPR4 cells, which allow them to adapt to the substratum for efficient migration when adherent and generate more spontaneous protrusions when in suspension. Comparing the quantitative 3D data for these cells in suspension with those of the attached cells, we established clearly the fact that the inhibition of spontaneous protrusions in the B16/GPR4 cells can indeed reduce their ability to migrate significantly. One should note that the numbers of R_c sampling for the histograms were kept as the same at 1000 between the minimum and maximum values of R_c for each cell with nonzero values of cell surface voxel number N_{sc}. So the mean values of the total number of N_{sc} for each cell groups are approximately the same and are consistent with those of the cell surface area S_c in Table 1 even though the areas under curves in Fig. 5 appear quite different.

The quantitative results of 3D morphological study also reveal several interesting features related to the potential effects of GPR4 on the B16F10 cells. The inhibition of cell protrusions by GPR4 has been correlated with its putative function in the regulation of cell migration and cytoskeleton.[8] The results presented in Table 1 further indicate that both mitochondrial volume and surface to volume ratio increase significantly in B16/GPR4 cells relative to both of the B16/vector and B16 cells, which may affect cell respiration. To further understand the effect of these structural variations, the mitochondrial respiration of B16F10 melanoma cells was measured using 5 samples for each cell type. This enabled us to examine whether the maximal capacity of mitochondrial oxygen consumption rate (OCR) is different between the two cell lines for possible correlation to their morphological differences. Cells were treated with the mitochondrial uncoupler FCCP and the maximal OCR was measured using the Seahorse XF analyzer as described in the Methods section. Fig. 6 shows that the maximal OCR of B16/GPR4 cells are approximately 20–30% higher than that of B16/vector cells ($p < 0.01$). These results can be compared with the values of mitochondrial parameters in Table 1 where the volume V_m, surface S_m and surface to volume ratio SVr_m of the B16/GPR4 cells are all significantly larger than those of the B16/vector cells. A more detailed reading of the parameter distributions for the two cell types as presented in Fig. 7 provides some interesting observations on the effect of GPR4. In comparison with the B16/GPR4 cells, the B16/vector cells are much more heterogeneous in their distributions of the mitochondria parameters. Since both

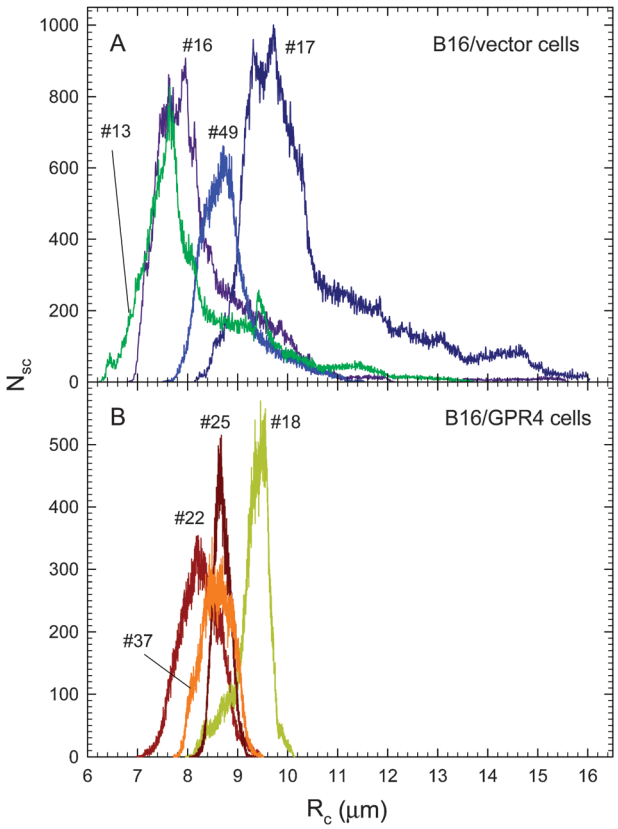

Fig. 5 Histograms of the cell surface voxel number N_{sc} of 4 cells in the groups of (A) B16/vector; (B) B16/GPR4 with R_c as the radial distance between cell surface voxels and the centroid of cell. Each curve is labeled by the cell sequence number in its group with two shown in Fig. 1 and 2.

surface area S_m and index of surface irregularity ISI_m are proportional to the numbers of voxels on the mitochondria membrane, they distribute roughly along a line representing their linear dependence on mitochondrial volume V_m for majority of the B16/GPR4 cells. Hence one can quickly realize that not only do the B16/vector cells deviate from the line towards the region of smaller V_m but they tend to have smaller S_m than their B16/GPR4 counterparts having the same V_m. This leads to the significant difference in the surface to

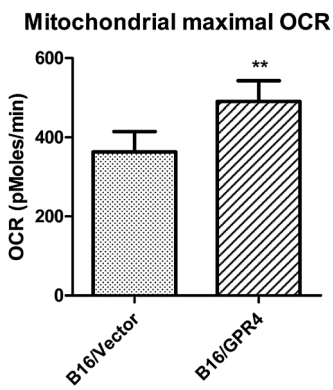

Fig. 6 Maximum mitochondrial oxygen consumption rates (OCR) between the B16/GPR4 and B16/vector cells measured with 5 samples for each cell type and ** indicating $p < 0.01$ by t-test.

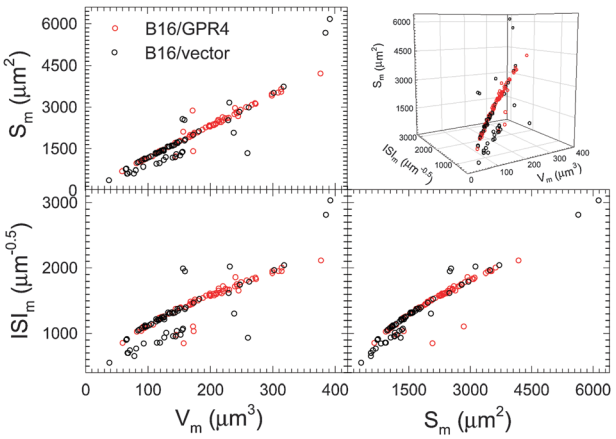

Fig. 7 2D and 3D scatter plots of mitochondrial parameters of surface area S_m, volume V_m and index of surface irregularity ISI_m for the B16/vector and B16/GPR4 cells.

volume ratio of mitochondria SVr_m for the different cell types as shown in Table 1. We may further remark that difference in SVr_m may have more bearing on the results in Fig. 6 than the difference V_m because the former could markedly influence the uptake and release of metabolically important molecules including oxygen during the OCR measurements, as well known for other organelles.[24] Nevertheless the molecular basis of the above observations with cells conditioned differently remains to be fully investigated.

Discussion and conclusions

Our results based on both of the 3D morphological analysis and functional measurement yield several intriguing insights into how the acidic tumor microenvironment regulates cancer cell behavior through the proton-sensing GPR4 receptor beyond what was known.[8,25–28] First, acidosis stimulation of GPR4 affects actin subcellular localization and stress fiber formation in migrating B16F10 melanoma cells (Fig. 4B), inhibits cells' ability to generate protrusions and to spread (Fig. 2 and 3), and impairs the dynamics of lamellipodia formation and tail retraction (Fig. 4A and Videos S3 and S4, ESI†). These observations are consistent with the previously reported biological effects of GPR4 to inhibit tumor cell migration and metastasis and the biochemical function to activate the G13/Rho pathway upon acidic pH stimulation.[8,26] Furthermore, our preliminary results show that inhibiting the Rho GTPase by C3 transferase can partially rescue the attachment defect of B16/GPR4 cells (C.R.J and L.V.Y, unpublished observation). Second, our results have revealed a potentially novel molecular connection between the acidic tumor microenvironment and cancer cell metabolism. Decades ago Otto Warburg observed that cancer cells rely heavily on glycolysis rather than oxidative phosphorylation for ATP production and proposed that cancer cell mitochondria are defective and this defect serves as the cause of tumorigenesis.[29] Numerous studies published subsequently confirmed that glycolysis is commonly increased in many types of tumors.[4,30,31] Recent studies also demonstrated that glycolysis is directly regulated by some oncogenes and tumor suppressors and by adaptation to the

tumor microenvironment.[4,30–32] Contrary to Warburg's original proposal, however, the respiration capacities of many cancer cells are not defective per se but instead inhibited by certain molecular mechanisms.[32–34] Here we observed that overexpression of the GPR4 receptor in B16F10 melanoma cells increases the total volume and surface to volume ratio of mitochondria which is corroborated by an increase in maximal capacity of mitochondrial OCR. Further research is therefore warranted to investigate the detailed molecular mechanisms by which the acidic tumor microenvironment and the proton-sensing GPR4 receptor regulate the metabolism of cancer cells and how cell metabolism is potentially related to cancer metastasis.[35] Third, we have developed an efficient and powerful approach to utilize the readily available confocal microscopy method for quantitative characterization and analysis of the 3D morphology of cells and subcellular organelles. Even though the quantitative results of morphology were obtained from detached cells in suspension, it has been shown that these results are consistent with the functional analyses of cell migration and respiration under the adherent condition. Still we need to point out that the results obtained from cells conditioned differently are of indirect nature and subsequent interpretations need to be carefully verified with further studies. Finally, we have demonstrated that the approach of 3D morphological analysis presented here can serve as a valuable tool for the study of cell functions. The presented approach of imaging and reconstruction is also sufficiently robust to be extended to different subcellular organelles with appropriate fluorescence labeling dyes and help lay the foundation for development of other morphology based methods of cell assay.

Methods

Three types of B16F10 cells

The culture of malignant mouse B16F10 melanoma cells and the generation of the genetically engineered B16/vector cells and B16/GPR4 cells have been previously described.[8] Briefly, B16F10 melanoma cells were stably transduced with the MSCV-GPR4-IRES-GFP retroviral construct to over-express the wild-type human GPR4 receptor or with the MSCV-IRES-GFP vector as a control. The two genetically engineered cell lines are called as B16/GPR4 and B16/vector cells, respectively.

Confocal imaging

The cells to be imaged were first detached from culture plates using trypsin/EDTA followed by staining. The fluorescent dyes of Syto 61 and MitoTracker Orange (Life Technologies) were chosen for staining the nucleus and mitochondria of the live cells, respectively. After incubation in culture media with the two dyes for 30 minutes at 37 °C followed by one wash, the cells were loaded in clear culture medium between a dipped glass slide and cover glass as a suspension sample for imaging with a laser scanning confocal microscope (LSM510, Zeiss). We employed a 63× water-immersion objective with a 4× scan zoom on the acquired image slices. Each image stack consisted of about 40 to 60 slices with a 0.5 μm step size in air along the z-axis.

Image segmentation. Segmentation started with a histogram analysis to select two thresholds of pixel intensity I for segmentation. To reduce fluctuations, pixels of all slices in the image stack were pooled in each false-color channel to produce a histogram. As shown in Fig. 1(B), the largest peak of the histogram occurs at or near $I = 0$ in both of the red and green channels since most extracellular pixels are of lowest intensities. Consequently we used the first minimum after the above peak as a reliable threshold of I_1 to zero most extracellular pixels of $I < I_1$. The intensity of the next peak in the histogram I_2 was picked as the second threshold to identify the intracellular and mitochondria pixels in the red and green channels, respectively. The two thresholds are indicated with arrows in each histogram curve in Fig. 1B. After the histogram analysis was done for each of the two channels, slices in each channel were then processed separately for segmentation of different organelles before they are recombined to output the final 3D structure files.

The borderlines representing the membranes of cell and nucleus were obtained in each slice by iterating the following algorithms. A Sobel operator was used to derive the spatial gradient slices of dI for detection of edges in the cleaned slices stack to identify the cell membrane. From the gradient images two derivative thresholds of dI_1 and dI_2 were chosen to mark the cytoplasm and nuclear membranes and obtain two binary stacks respectively. The first binary stack assigns the intensity $I = 1$ for all pixels with either derivative $dI > dI_1$ as those on the cytoplasmic membrane or with $I > I_1$ as the intracellular pixels and $I = 0$ for rest of the pixels as the background. The other binary stack of nucleus was obtained similarly except dI_2 replaces dI_1. The two binary stacks were further refined with opening and closing operations to remove the "wrong" pixels in the regions separated by the borderline of membrane.[36] In the green channel the cytoplasm membrane was first detected to output a binary stack. The two cytoplasm stacks from the two channels were compared and the one with larger areas in each slice was selected as the final output. For accurate segmentation of mitochondria, additional algorithms had to be employed because of their much smaller sizes, which include adaptive median filtering with auto-adjusted window size for smoothing and watershed algorithms to increase the accuracy in delineating clusters within aggregated mitochondria pixels.[37,38] The final step was to combine the segmented stacks of cytoplasm, nucleus and mitochondria into an 8-bit gray-scale stack in which each pixel was given an intensity as an index of organelle and fluorescence intensity bin. Fig. 1(A) presents the raw confocal and segmented slices selected from a stack.

3D reconstruction

After segmentation additional slices were added through interpolation to obtain a stack with cubic voxels. Because of the refraction of the fluorescence light at various interfaces from the emitting molecules to the microscope objective, the distance of sample translation $\Delta z'$ is larger than the actual slice separation Δz in the raw image stack.[39] Using fluorospheres of nominal diameter at 10 μm under the same confocal imaging conditions we have determined the correction factor to be $f = \Delta z/\Delta z' = 0.862$ by requiring isotropic diameters for the microsphere.

Following the z-axis calibration 5 slices were added between the neighboring slices using a shape-based interpolation algorithm.[40] With this method, we calculated a signed shortest distance of each pixel at (x, y) in a segmented slice to the membrane of a particular organelle of cytoplasm, nucleus and mitochondria. The sign was determined by if the pixel is inside the organelle. For each interpolated slice the signed shortest distance of each pixel at (x, y) is obtained by averaging the two distances of the pixels at (x, y) in the two segmented slices neighboring the new one with weights proportional to the separations between the new and segmented slices. The organelle membrane in the new slice could thus be identified by those pixels of zero distances. For confocal image stacks with up to 60 slices, the typical calculation times of 3D reconstruction on a 2 GHz dual-core PC ranged from 10 to 15 minutes. After reconstruction multiple 3D morphological parameters were calculated for the organelles of cytoplasm, nucleus and mitochondria and values of selected parameters are presented in Table 1. The notes under Table 1 provide the parameter definitions.

Cell attachment and migration assays

B16/Vector and B16/GPR4 cells were detached from culture plates using trypsin/EDTA. After washed once with media, cells were resuspended in culture media, added onto a glass coverslip and incubated in a sealed chamber with 5% CO_2 at 37 °C. Cell attachment was recorded in real-time using a time-lapse digital inverted phase microscope (EVOS, Advanced Microscopy Group) after cell plating over a time course of 1 h. For the migration assays B16/Vector and B16/GPR4 cells were cultured to 100% confluence in 6-well plates. A wound of the cell monolayer was generated using a pipette tip and the cells were then incubated in a sealed chamber with 5% CO_2 at 37 °C. Cell migration was recorded for 16 h. Four video files made out of these images are provided in the ESI.† The images were used to analyze the morphological features of migrating cells and to identify the edges of the wound with a threshold based image processing algorithm. The vertical wound in the images was divided into 17 bands of equal height and 5 rows of pixels in each band were used to obtain the average width of the wound in that band after image processing and edge detection. Compilation of the wound width or distance between the edges of the monolayer on two sides of the wound width among the time-lapsed images yielded the cell migration data as a function of time at multiple locations along the edges to quantify cell migration dynamics. Actin cytoskeleton staining was applied to cells grown on a glass coverslip which were fixed with 4% formaldehyde for 10 min, and the rhodamine phalloidin staining of actin cytoskeleton was performed as previously described.[8]

Measurement of mitochondrial OCR

We measured the oxygen consumption rate (OCR) of B16/Vector and B16/GPR4 cells with an extracellular flux analyzer (XF24, Seahorse Bioscience Inc.) by following the manufacturer's instruction. Briefly, 10 000 cells per well were seeded into the 24-well Seahorse microplates and cultured with DMEM + 10% FBS media overnight. The next day, cells were switched to the assay buffer (DMEM without bicarbonate or HEPES) and treated with 0.5 μM uncoupler FCCP (Carbonyl cyanide-*p*-trifluoromethoxyphenylhydrazone) to allow maximal cell respiration. The maximal total OCR was measured using the flux analyzer. Then cells were treated with 1 μM antimycin A and 1 μM rotenone to measure non-mitochondrial OCR which was subtracted from the total OCR to calculate the maximal mitochondrial OCR. Data were normalized by total protein using the sulforhodamine B assay (Sigma-Aldrich). Five groups of samples were measured for each cell type to obtain the mean values and standard error of the mean (SEM).

Statistical analysis

The method of two-sample t-test was chosen for examination of the morphological similarity among the three types of B16 cells. The statistical method allows the testing of equality of means between two selected cell types of equal or unequal variances. The two-sample t-tests of the parameters in Table 1 were performed with the SPSS software (Version 19, IBM) to obtain the values of p_{12} and p_{23}, respectively, for each 3D parameters between two cell types as noted in the table. The OCR data in Fig. 6 was analyzed using the t-test with the Prism software (Version 5, GraphPad Software).

The authors declare no conflict of interest.

Acknowledgements

We thank Junhua Ding and Carrisa L. Reynolds for participation in early algorithm development, Andrew E. Ekpenyong and Carrisa L. Reynolds for acquiring some of the confocal image stacks of the B16F10 cells used in this study, and Lixue Dong and Nancy Leffler for technical assistance. Y.F. acknowledges the grant support by the National Science Foundation of China (grant #81171342). L.V.Y acknowledges the grant supports from North Carolina Biotechnology Center, Brody Brothers Endowment Fund, Golfers against Cancer, and the American Heart Association.

References

1 D. A. W. Thompson, *On growth and form*, Cambridge University Press, Cambridge, United Kingdom, 1961.
2 J. M. Bennett, D. Catovsky, M.-T. Daniel, G. Flandrin, D. A. G. Galton, H. R. Gralnick and C. Sultan, *Br. J. Haematol.*, 1976, **33**, 451–458.
3 C. S. Reynolds, V. Huszar, C. Kruk, L. Naselli-Flores and S. Melo, *J. Plant Res.*, 2002, **24**, 417–428.
4 R. A. Gatenby and R. J. Gillies, *Nat. Rev.*, 2004, **4**, 891–899.
5 D. Hanahan and R. A. Weinberg, *Cell*, 2011, **144**, 646–674.
6 L. V. Yang, R. D. Castellone and L. Dong, in *Cancer Prevention-From Mechanisms to Translational Benefits*, ed. A. G. Georgakilas, InTech, 2012, pp. 3–40.
7 I. J. Fidler and G. Poste, *Lancet Oncol.*, 2008, **9**, 808.
8 R. D. Castellone, N. R. Leffler, L. Dong and L. V. Yang, *Cancer Lett.*, 2011, **312**, 197–208.
9 K. M. Jacobs, L. V. Yang, J. Ding, A. E. Ekpenyong, R. Castellone, J. Q. Lu and X. H. Hu, *J. Biophotonics*, 2009, **2**, 521–527.
10 K. M. Jacobs, J. Q. Lu and X. H. Hu, *Opt. Lett.*, 2009, **34**, 2985–2987.
11 K. Dong, Y. Feng, K. M. Jacobs, J. Q. Lu, R. S. Brock, L. V. Yang, F. E. Bertrand, M. A. Farwell and X. H. Hu, *Biomed. Opt. Express*, 2011, **2**, 1717–1726.

12 J. R. Mourant, T. M. Johnson, V. Doddi and J. P. Freyer, *J. Biomed. Opt*., 2002, **7**, 93–99.
13 J. Q. Lu, P. Yang and X. H. Hu, *J. Biomed. Opt*., 2005, **10**, 024022.
14 R. S. Brock, X. H. Hu, D. A. Weidner, J. R. Mourant and J. Q. Lu, *J. Quant. Spectrosc. Radiat. Transfer*, 2006, **102**, 25–36.
15 H. Ding, J. Q. Lu, R. S. Brock, T. J. McConnell, J. F. Ojeda, K. M. Jacobs and X. H. Hu, *J. Biomed. Opt*., 2007, **12**, 034032.
16 S. B. Zimmerman and B. H. Pheiffer, *PNAS*, 1981, **78**, 78–82.
17 H. Jiang, C. Song, C. C. Chen, R. Xu, K. S. Raines, B. P. Fahimian, C. H. Lu, T. K. Lee, A. Nakashima, J. Urano, T. Ishikawa, F. Tamanoi and J. Miao, *PNAS*, 2010, **107**, 11234–11239.
18 J. B. Pawley, *Handbook of biological confocal microscopy*, Plenum Press, New York, 1995.
19 D. R. Soll, *Comput. Med. Imaging. Graph*., 1999, **23**, 3–14.
20 W. Choi, C. Fang-Yen, K. Badizadegan, R. R. Dasari and M. S. Feld, *Opt. Lett*., 2008, **33**, 171–173.
21 V. Nandakumar, L. Kelbauskas, R. Johnson and D. Meldrum, *Cytometry, Part A*, 2011, **79**, 25–34.
22 L. Schermelleh, P. M. Carlton, S. Haase, L. Shao, L. Winoto, P. Kner, B. Burke, M. C. Cardoso, D. A. Agard, M. G. Gustafsson, H. Leonhardt and J. W. Sedat, *Science*, 2008, **320**, 1332–1336.
23 X. T. Su, K. Singh, C. Capjack, J. Petracek, C. Backhouse and W. Rozmus, *J. Biomed. Opt*., 2008, **13**, 024024.
24 W. M. Lewis, *Science*, 1976, **192**, 885–887.
25 A. Chen, L. Dong, N. R. Leffler, A. S. Asch, O. N. Witte and L. V. Yang, *PLoS One*, 2011, **6**, e27586.
26 M. G. Ludwig, M. Vanek, D. Guerini, J. A. Gasser, C. E. Jones, U. Junker, H. Hofstetter, R. M. Wolf and K. Seuwen, *Nature*, 2003, **425**, 93–98.
27 X. Sun, L. V. Yang, B. C. Tiegs, L. J. Arend, D. W. McGraw, R. B. Penn and S. Petrovic, *J. Am. Soc. Nephrol*., 2010, **21**, 1745–1755.
28 L. V. Yang, C. G. Radu, M. Roy, S. Lee, J. McLaughlin, M. A. Teitell, M. L. Iruela-Arispe and O. N. Witte, *Mol. Cell. Biol*., 2007, **27**, 1334–1347.
29 O. Warburg, *Science*, 1956, **123**, 309–314.
30 M. G. Vander Heiden, L. C. Cantley and C. B. Thompson, *Science*, 2009, **324**, 1029–1033.
31 R. A. Cairns, I. S. Harris and T. W. Mak, *Nat. Rev. Cancer*, 2011, **11**, 85–95.
32 W. H. Koppenol, P. L. Bounds and C. V. Dang, *Nat. Rev. Cancer*, 2011, **11**, 325–337.
33 M. Barbi de Moura, G. Vincent, S. L. Fayewicz, N. W. Bateman, B. L. Hood, M. Sun, J. Suhan, S. Duensing, Y. Yin, C. Sander, J. M. Kirkwood, D. Becker, T. P. Conrads, B. Van Houten and S. J. Moschos, *PLoS One*, 2012, **7**, e40690.
34 I. Marin-Valencia, C. Yang, T. Mashimo, S. Cho, H. Baek, X. L. Yang, K. N. Rajagopalan, M. Maddie, V. Vemireddy, Z. Zhao, L. Cai, L. Good, B. P. Tu, K. J. Hatanpaa, B. E. Mickey, J. M. Mates, J. M. Pascual, E. A. Maher, C. R. Malloy, R. J. DeBerardinis and R. M. Bachoo, *Cell Metab*., 2012, **15**, 827–837.
35 B. Bhandary, A. Marahatta, H. R. Kim and H. J. Chae, *J. Bioenerg. Biomembr. (e-pub)*, 2012, DOI: 10.1007/s10863-012-9464-x.
36 R. M. Haralick, S. R. Sternberg and X. Zhuang, *IEEE Trans. Pattern Anal. Mach. Intell*., 1987, **PAMI–9**, 532–550.
37 H. L. Eng and K. K. Ma, *IEEE Trans. Image Process*., 2001, **10**, 242–251.
38 L. Vincent and P. Soille, *IEEE Trans. Pattern Anal. Mach. Intell*., 1991, **13**, 583–598.
39 T. D. Visser and J. L. Oud, *Scanning*, 1994, **16**, 198–200.
40 S. P. Raya and J. K. Udupa, *IEEE Trans. Med Imaging*., 1990, **9**, 32–42.

